Solar Energy Materials and Solar Cells 174 (2018) 405–411

Contents lists available at ScienceDirect

Solar Energy Materials and Solar Cells

journal homepage: www.elsevier.com/locate/solmat

Colloidal quantum dot solar cell electrical parameter non-destructive quantitative imaging using high-frequency heterodyne lock-in carrierography and photocarrier radiometry

Lilei Hu[a], Mengxia Liu[b], Andreas Mandelis[a,b,*], Qiming Sun[a], Alexander Melnikov[a], Edward H. Sargent[b]

[a] Center for Advanced Diffusion-Wave and Photoacoustic Technologies (CADIPT), Department of Mechanical and Industrial Engineering, University of Toronto, Toronto, Ontario, Canada, M5S 3G8

[b] Edward S. Rogers Sr. Department of Electrical and Computer Engineering, University of Toronto, Toronto, Ontario, Canada, M5S 3G4

ARTICLE INFO

Keywords:
Colloidal quantum dots (CQDs)
Solar cell
Carrier transport dynamics
Trap states
Carrier lifetime
Large-area imaging

ABSTRACT

Colloidal quantum dot (CQD) solar cells with a certified power conversion efficiency of 11.28% were characterized using camera-based heterodyne lock-in carrierography (HeLIC) and photocarrier radiometry (PCR). Carrier lifetime, diffusivity, and diffusion and drift length of a CQD solar cell were imaged in order to investigate carrier transport dynamics, as well as solar cell homogeneity and the effects of Au contacts on carrier transport dynamics. Using room temperature HeLIC imaging which has also been demonstrated using PCR measurements, shorter carrier lifetimes (ca. 0.5 μs) were found in Au contact regions that can be attributed to enhanced non-radiative recombinations through trap states at Au/CQD interfaces. This imaging methodology shows strong potential for elucidating the energy loss physics of CQD solar cells and for industrial non-destructive large-area photovoltaic device characterization.

1. Introduction

Colloidal quantum dots (CQDs) with tunable bandgap through effective control over CQD sizes have become promising candidates for fabricating low-cost, large-area, flexible, and lightweight solar cells [1–6]. Although CQD solar cell efficiencies have been boosted to 13.4% [7], there is still space for further improvement for commercial applications. Therefore, understanding of CQD solar cell energy loss mechanisms through factors such as film/contact interfaces [2,8], inefficient electrode collection of carriers [2,6], various trap states [9–12], CQD size polydispersity [13–15], and CQD bandtail states which deteriorate open-circuit voltage and inhibit carrier transport [1,6], is necessary for future photovoltaic device optimization.

Nowadays, large-area photovoltaic solar cells prevail, the characterization of which fulfills various purposes including shading effects, fundamental carrier transport dynamics, mechanical and electrical defect evaluation. Therefore, large-area characterization methodologies are needed for CQD solar cell efficiency optimization. Spatially resolved photoluminescence (PL) and electroluminescence (EL) constitute powerful methodologies for the characterization of silicon wafers [16–18] and solar cells [18–21]. They yield measurements of minority carrier hopping lifetime [16,17,20], open-circuit voltage [18,20,21], current density [21], series resistance [21], fill factor [18,21], and quality monitoring in different device fabrication steps [19]. Furthermore, due to the high signal-to-noise ratio (SNR), synchronous frequency-domain imaging methodologies are emerging, such as the lock-in thermography (LIT) [22] that has been used for determining series resistance and recombination current at a frequency of 20 Hz. However, static (dc) PL and EL, and low-frequency LIT limited by the low camera frame rate, cannot monitor electronic transport kinetics and recombination dynamics. The latter, however, are key parameters for the determination of photovoltaic energy conversion and dissipation.

To address these critical issues, here we introduce single detector-based photocarrier radiometry (PCR), and camera-based homodyne (HoLIC) and heterodyne (HeLIC) lock-in carrierographies for the characterization CQD solar cells. HoLIC imaging and PCR are the same type of dynamic spectrally gated frequency-domain photoluminescence modality and can yield quantitative information about carrier transport dynamics with accuracy and precision superior to the time-resolved PL due to their intrinsically high signal-to-noise ratio (SNR) by virtue of

* Corresponding author at: Center for Advanced Diffusion-Wave and Photoacoustic Technologies (CADIPT), Department of Mechanical and Industrial Engineering, University of Toronto, Toronto, Ontario, Canada, M5S 3G8.
E-mail address: mandelis@mie.utoronto.ca (A. Mandelis).

http://dx.doi.org/10.1016/j.solmat.2017.09.020
Received 26 April 2017; Received in revised form 29 July 2017; Accepted 11 September 2017
Available online 25 September 2017
0927-0248/

lock-in demodulation [23,24]. HoLIC has advantages as an all-optical non-destructive imaging technique for large-area photovoltaic device imaging, yet it is limited to the low modulation frequency range (< 1 kHz) due to the low frame rates of conventional cameras [25]. Using a single InGaAs detector, PCR can attain high-frequency characterization (> 100 kHz), however, the fast large-area imaging capability is compromised. Through creating a slow enough beat frequency component, HeLIC overcomes the high-frequency limitation of conventional camera-based optical characterization techniques and the poor SNR at short exposure times associated with high frame rates [26] to realize frequency-modulated imaging at more than 100 kHz. Therefore, with higher SNR than dc PL imaging, HeLIC can attain a wide range of frequency-dependent ac carrier diffusion lengths to generate depth-selective/resolved high-frequency imaging of carrier transport parameters in large-scale devices. It should be noted that all three techniques (PCR, HoLIC, and HeLIC) have no low-frequency limitations.

Therefore, to study carrier transport dynamics in CQD solar cells and the effects of CQD layer inhomogeneity (for example, induced at various fabrication stages) and contact/film interface effects on solar cell performance, we combined a *J-V* model with PCR and HeLIC to quantitatively produce carrier lifetime, diffusivity, and drift and diffusion length images for a high-efficiency CQD solar cell under frequency modulated excitation. This methodology has a strong potential impact on solar cell efficiency optimization and on industrial non-destructive solar cell quality control.

2. Theoretical methods

2.1. Solar cell under harmonic excitation

The nature of photocarrier generation, discrete hopping transport, and recombination in CQD-based thin films was found to follow a hopping diffusion transport behavior [2,27] under frequency-modulated laser excitation that reveals details of carrier hopping transport dynamics in these photovoltaic materials. Here, in order to extract charge carrier hopping transport dynamics in CQD-based solar cells Fig. 1(a), light-matter interaction under modulated-frequency excitation is investigated as an extension of conventional current-voltage characterization of CQD solar cells under dc laser excitation [2,6,28]. Reviewing the CQD solar cell structure in Fig. 1, due to the larger bandgap energy of ZnO than the incident excitation photon energy and the thicker CQD layers than ZnO, charge carriers and excitons are considered to be generated only in CQD layers, thus contributing to the primary current within this type of solar cell. In a manner similar to the carrier hopping transport model under static excitation [2], as electrons are injected from CQD layer to the electron-accepting ZnO nanoparticles [1], the rate equation for electrons in the CQD layers under dynamic illumination can be written as

$$\frac{\partial \Delta n(x,t)}{\partial t} = \frac{\partial J_e(x,t)}{\partial x} - \frac{\Delta n(x,t)}{\tau} + g(x,t) \tag{1}$$

$\Delta n(x,t)$ is the excess electron density and $J_e(x,t)$ is the electron current flux; τ is the electron carrier lifetime, and $g(x,t)$ is the carrier generation rate. Considering that the ambipolar diffusion coefficient and mobility, $J_e(x,t)$ can be further defined by [29,30]

$$J_e(x,t) = D_e \frac{\partial \Delta n(x,t)}{\partial x} + \mu_e E \Delta n(x,t) \tag{2}$$

where D_e is the diffusivity, μ_e is the mobility, and E is the electric field (a constant value given as the difference between the external and intrinsic electric fields), Eq. (1) is reduced to a diffusion equation which can be solved using the Green function method and transferred to the frequency domain through a Fourier transformation [29]. Upon harmonic optical excitation, the photoexcited excess carrier distribution follows the Beer-Lambert Law:

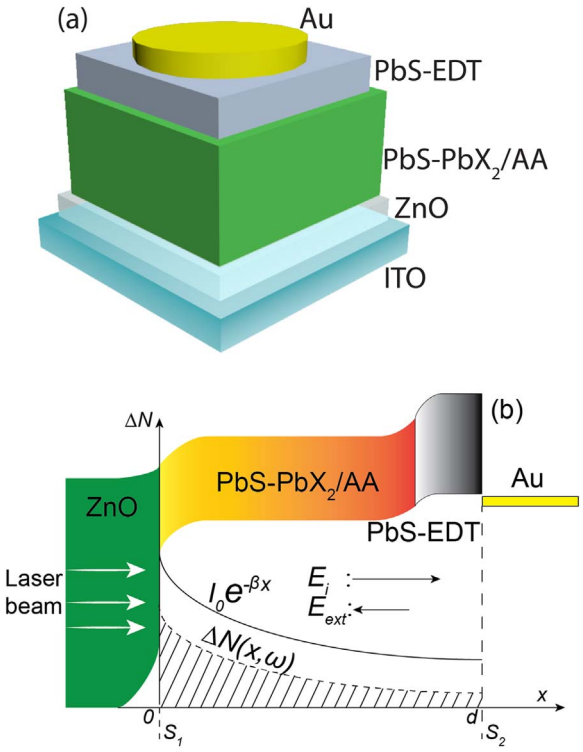

Fig. 1. Schematic of CQD solar cell sandwich structure (a), and the corresponding band energy structure (b) that shows the illumination depth profile, the photocarrier density wave distribution and the intrinsic and external electric fields.

$$g(x,\omega) = \frac{\beta \eta I_0}{2h\nu} e^{-\beta x}(1+e^{i\omega t}) \tag{3}$$

where β is the optical absorption coefficient, η is the quantum yield of the photogenerated carriers, and h and ν are the Plank constant and the frequency of incident photons, respectively. I_0 denotes the incident photon intensity. In the one-dimensional geometry, the boundary conditions at $x = 0$ and d, Fig. 1(b), can be written as functions of surface recombination velocities (S_1 and S_2 at $x = 0$ and $x = d$, respectively,) and the excess carrier density at the corresponding boundaries.

$$D_e \frac{\partial \Delta N(x,\omega)}{\partial x}\bigg|_{x=0} = S_1 \Delta N(0,\omega) \tag{4a}$$

$$-D_e \frac{\partial \Delta N(x,\omega)}{\partial x}\bigg|_{x=d} = S_2 \Delta N(d,\omega) \tag{4b}$$

where $\Delta N(x,\omega)$ is the Fourier transform $\Delta n(x,t)$, a carrier-density-wave (CDW). Therefore, the final expression of harmonic excess carriers $\Delta N(x,\omega)$ can be obtained as follows

$$\begin{aligned}\Delta N(x,\omega) = \frac{\eta I_0 \beta}{4h\nu D_e(1 - R_{e1}R_{e2}e^{-2K_e d})[\beta^2 - (Q_0^2 + \sigma_e^2)]}\{\big([(1+\rho_e) \\ - R_{e1}(1-\rho_e)] - R_{e1}[(\rho_e - 1) + R_{e2}(1+\rho_e)]e^{-(K_e+\beta)d}\big)e^{-K_e x} \\ + \big(R_{e2}[(1+\rho_e) - R_{e1}(1-\rho_e)] \\ + [(1-\rho_e) - R_{e2}(1+\rho_e)]e^{-(\beta-K_e)d}\big)e^{-K_e(2d-x)} \\ -2\big(1 - R_{e1}R_{e2}e^{-2K_e d}\big)e^{-\beta x}\}\end{aligned} \tag{5}$$

with the following definitions,

$$\overrightarrow{Q_0} = \frac{\mu_e}{2D_e}\overrightarrow{E}\ [\mathrm{cm}^{-1}]; \sigma_e = \sqrt{\frac{1+i\omega\tau}{D_e\tau}}\ [\mathrm{cm}^{-1}] \tag{6a}$$

$$R_{ej} = \frac{D_e\sqrt{Q_0^2 + \sigma_e^2} - S_j}{D_e\sqrt{Q_0^2 + \sigma_e^2} + S_j}, j = 1, 2 \tag{6b}$$

$$K_e = \sqrt{Q_0^2 + \sigma_e^2} - Q_0 [\mathrm{cm}^{-1}]; \rho_e = \frac{\beta}{K_e} \tag{6c}$$

As shown in Fig. 1(b), the electric field $\vec{E} = \vec{E}_i + \vec{E}_{ext}$ ($E_i > E_{ext}$) prevents the spreading of the excess CDW density towards the $x = d$ terminal of the solar cell. On the contrary, when the net electric field switches its direction it facilitates the spreading of the CDW concentration gradient, resulting in reduced energy barriers. Here, all discussion will be based on the condition that $\vec{E}$ prevents the spreading of the excess electron CDW density, i.e. $\vec{E}$ and $\vec{E}_i$ have the same direction, which is a general working condition for traditional solar cells.

2.2. Homodyne and heterodyne lock-in carrierographies

The InGaAs camera based HoLIC and HeLIC methods collect photons from radiative recombination of charge CDWs or excitons in CQD photovoltaic materials and devices. The recombination rate (R_R) is proportional to the product of the concentration of electrons n and holes p in the form of $R_R = knp$ [31], where k is a material-dependent constant which can be obtained from the semiconductor's absorption coefficient. Using the CDW $\Delta N(x, \omega)$ in the frequency domain, the homodyne and heterodyne signals can be modeled through a depth integral of the radiatively recombining free photocarrier densities:

$$S(\omega) = \int_0^d dx \int_{\lambda_1}^{\lambda_2} \Delta N(x, \omega)[\Delta P(x, \omega) + N_A] F(\lambda) d\lambda \tag{7}$$

where $\Delta P(x, \omega)$ is the excess hole CDW and equals $\Delta N(x, \omega)$ according to the quasi-neutrality approximation, i.e. the photogenerated excess electron and hole concentrations are identical across the thin film thickness. $F(\lambda)$ is an instrumental coefficient that depends on the spectral detection bandwidth (λ_1, λ_2) of the near-infrared detector. N_A is the equilibrium majority carrier concentration determined by material doping resulting from in-air oxidation of our CQD thin films and solar cells. PCR and HoLIC detect at only the fundamental reference frequency term. In comparison, in HeLIC the incident laser excitation is modulated at two different angular frequencies ω_1 and ω_2. Furthermore, HeLIC is tuned to the reference beat frequency $\Delta\omega = |\omega_2 - \omega_1|$, so that radiative recombination modulated at other frequencies will be filtered out. The demodulated signal for PCR and HoLIC can be derived using

$$\Delta N(x, \omega) = \Delta n_0(x) + Y(x, \omega) \exp\{i[\omega t + \varphi(x, \omega)]\} \tag{8}$$

in which $Y(x, \omega)$ and $\varphi(x, \omega)$ are the amplitude and phase of the frequency modulated CDW, respectively, and $\Delta n_0(x)$ is the corresponding dc component. The final signal expression for PCR and HoLIC is

$$S_{ho}(\omega) = \int_0^d (2\Delta n_0(x) + N_A) \Delta N(x, \omega) dx \tag{9}$$

Similarly, the demodulated signal for HeLIC can be derived through

$$\begin{aligned} \Delta N(x, \omega) = {} & 2\Delta n_0(x) + Y(x,\omega_1) exp\{i[\omega_1 t + \varphi(x,\omega_1)]\} \\ & + Y(x,\omega_2) exp\{i[\omega_2 t + \varphi(x,\omega_2)]\} \end{aligned} \tag{10}$$

Therefore, the expression for the HeLIC signal becomes

$$S_{he}(\Delta\omega) = \int_0^d \Delta N^*(x, \omega_1) \Delta N(x, \omega_2) dx \tag{11}$$

where * denotes complex conjugation and $\Delta n_0(x)$ is the dc component of the photogenerated excess electron CDW $\Delta N(x, \omega)$. It should be noted that the HeLIC phase is very small (on the order of 0.001°) due to the small frequency difference $\Delta\omega$.

Ultimately, under low injection levels, i.e. $2\Delta n_0(x) \ll N_A$, upon substitution of Eq. (5) into Eq. (9), the final expression of Eq. (9) after the necessary mathematical manipulations becomes

$$S_{ho}(\omega) \approx AN_A \left[\frac{B(1-e^{-dK_e}) + C(e^{-dK_e} - e^{-2dK_e})}{K_e} + \frac{D(e^{-d\beta} - 1)}{\beta} \right] \tag{12}$$

Coefficients A, B, C, and D are defined according to Eq. (5), as follows,

$$A = \frac{\eta I_0 \beta}{4h\nu D_e (1 - R_{e1} R_{e2} e^{-2K_e d})[\beta^2 - (Q_0^2 + \sigma_e^2)]} \tag{13a}$$

$$B = [(1+\rho_e) - R_{e1}(1-\rho_e)] - R_{e1}[(\rho_e - 1) + R_{e2}(1+\rho_e)] e^{-(K_e+\beta)d} \tag{13b}$$

$$C = R_{e2}[(1+\rho_e) - R_{e1}(1-\rho_e)] + [(1-\rho_e) - R_{e2}(1+\rho_e)] e^{-(\beta - K_e)d} \tag{13c}$$

$$D = 2\left(1 - R_{e1} R_{e2} e^{-2K_e d}\right) \tag{13d}$$

Correspondingly, when combined with Eq. (5), the final expression of Eq. (11) is derived as follows

$$\begin{aligned} S_{he}(\Delta\omega) = \frac{1}{2\pi} A^*(\omega_1) A(\omega_2) \Bigg\{ & - \frac{B^*(\omega_1) B(\omega_2)[e^{-d[K_e^*(\omega_1) + K_e(\omega_2)]} - 1]}{K_e^*(\omega_1) + K_e(\omega_2)} \\ & + \frac{B^*(\omega_1) C(\omega_2)[e^{-d[K_e^*(\omega_1) + K_e(\omega_2)]} - e^{-2dK_e(\omega_2)}]}{-K_e^*(\omega_1) + K_e(\omega_2)} \\ & + \frac{B^*(\omega_1) D(\omega_2)[e^{-d[K_e^*(\omega_1) + \beta]} - 1]}{K_e^*(\omega_1) + \beta} \\ & + \frac{C^*(\omega_1) B(\omega_2)[e^{-d[K_e^*(\omega_1) + K_e(\omega_2)]} - e^{-2dK_e^*(\omega_1)}]}{K_e^*(\omega_1) - K_e(\omega_2)} \\ & + \frac{C^*(\omega_1) C(\omega_2)[e^{-d[K_e^*(\omega_1) + K_e(\omega_2)]} - e^{-2d[K_e^*(\omega_1) + K_e(\omega_2)]}]}{K_e^*(\omega_1) + K_e(\omega_2)} \\ & - \frac{C^*(\omega_1) D(\omega_2)[e^{-d[K_e^*(\omega_1) + \beta]} - e^{-2dK_e^*(\omega_1)}]}{K_e^*(\omega_1) - \beta} \\ & + \frac{D^*(\omega_1) B(\omega_2)[e^{-d[\beta + K_e(\omega_2)]} - 1]}{\beta + K_e(\omega_2)} \\ & - \frac{D^*(\omega_1) C(\omega_2)[e^{-d[\beta + K_e(\omega_2)]} - e^{-2dK_e(\omega_2)}]}{-\beta + K_e(\omega_2)} \\ & - \frac{D^*(\omega_1) D(\omega_2)[e^{-2\beta d} - 1]}{2\beta} \Bigg\} \end{aligned} \tag{14}$$

Here A^*, B^*, C^*, and D^* are the complex conjugates of A, B, C, and D, respectively, in Eq. (13).

Theoretically, it should be noted that as HeLIC detects ac PL modulated at the reference angular frequency $\Delta\omega$, the axial and radial spatial resolution of HeLIC is also determined by the angular modulation frequency ω through the ac diffusion length $L(\omega)$

$$L(\omega) = \sqrt{\frac{D_e \tau}{1 + i\omega\tau}} \tag{15}$$

Therefore, shorter $L(\omega)$ at higher angular modulation frequencies ω yields higher spatial resolution in the axial and radial directions for CQD solar cells.

3. Experimental details

Oleic-acid-capped CQDs and ZnO nanoparticles were synthesized following our previously published method [1]. As shown in Fig. 1, the CQD solar cells have a sandwich structure of PbS CQDs treated by two different ligands, i.e. PbX_2/AA (PbX_2: lead halide, AA: ammonium acetate) and EDT (1, 2-ethanedithiol). ZnO nanoparticles with a thickness of 120 nm were first spin-casted onto an indium tin oxide (ITO) glass, followed by the deposition of 350 nm PbX_2/AA-exchanged and 50 nm EDT-exchanged PbS CQDs. Eventually, a 120-nm Au thin film was thermally evaporated on the top as electrodes [1]. *J-V* characteristics were obtained using a Keithley 2400 source measuring instrument under simulated AM1.5 illumination in a nitrogen environment. The experimental setups for the camera-based HoLIC and HeLIC, as well as for the single detector based PCR, are presented in Fig. 2. The PCR system, Fig. 2(a), features an 808 nm laser diode optical source frequency-modulated using a function generator. An optical long-pass filter (Spectrogon LP-1000 nm) is mounted in front of the InGaAs single-element detector to block the excitation laser beam [25,26]. As shown in Fig. 2(b), HoLIC and HeLIC share the same experimental setup. They feature two laser diode systems and an InGaAs camera

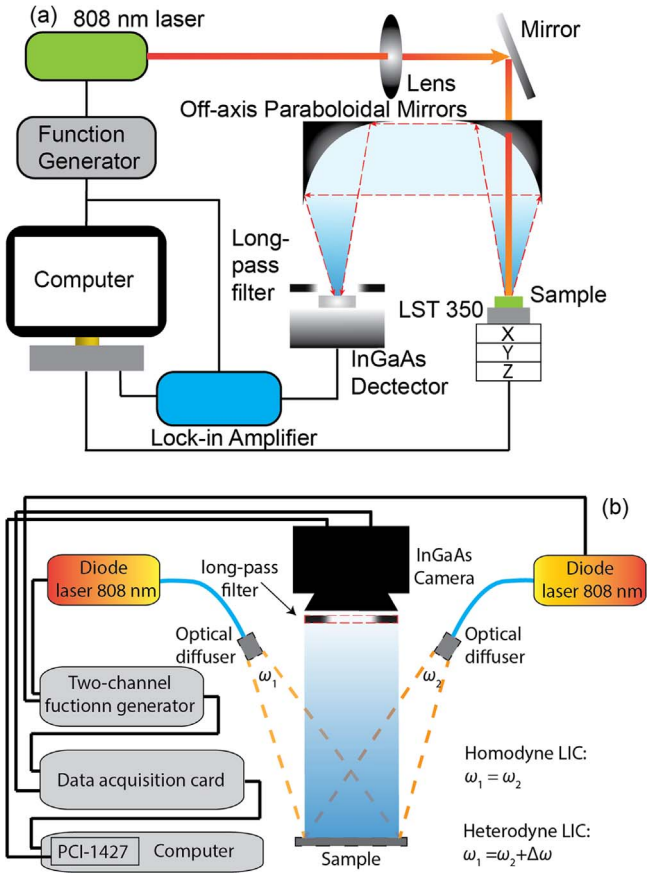

Fig. 2. Experimental setup for (a) photocarrier radiometry (PCR), and (b) homodyne (HoLIC) and heterodyne (HeLIC) lock-in carrierographies. LST 350 is the Linkam cryogenic stage that allowed maintaining constant temperatures in a range between 77 and 520 K for PCR temperature scans.

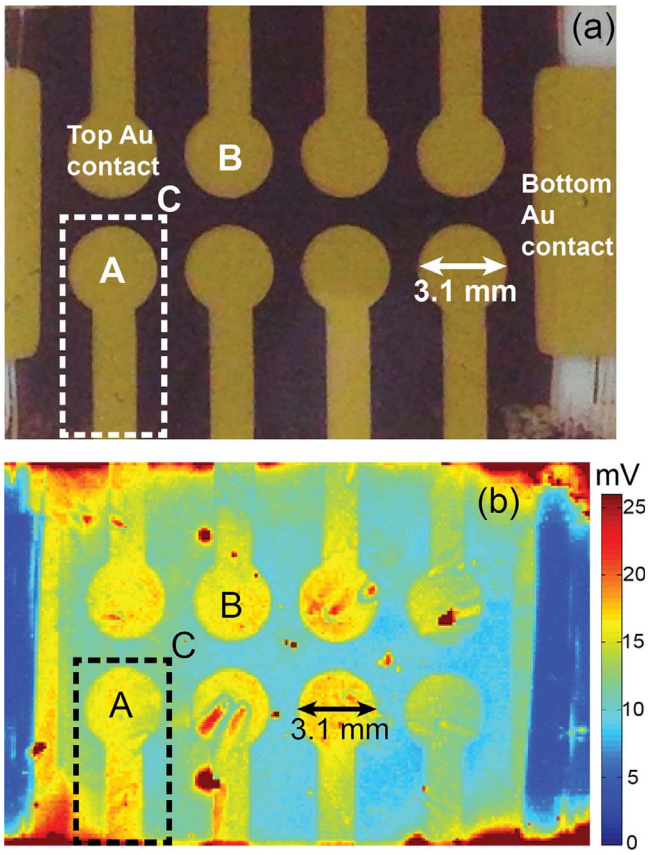

Fig. 3. (a) A photograph of the CQD solar cell sample under study, and (b) the corresponding HoLIC image of this solar cell. The dashed-rectangle-circumscribed solar cell A is selected for further studies as shown in Figs. 4 and 5. The HoLIC characterization was carried out at 10 Hz. It should be noted that for carrierographic imaging, the sample was flipped over with the top Au contact on the bottom.

rather than a single detector. The NIR InGaAs camera (Goodrich SU320 KTSW-1.7RT/RS170) has 320 × 256 pixel active elements with a bandwidth of 0.9–1.7 μm, 120 fps frame rate, and exposure times between 0.13 and 16.6 ms. The number of camera pixels determines the spatial resolution of both HoLIC and HeLIC imaging techniques. The two diode lasers with the same excitation power deliver a combined mean laser excitation intensity of 1 sun. An optical long-pass filter is also mounted in front of the InGaAs camera to block the excitation laser beam. In order to obtain homogeneous excitation, two optical diffusers are used to minimize the intensity variation across the beam (< 5%). When the two lasers are modulated at the same frequency and in phase, HoLIC imaging is obtained (amplitude and phase images), whereas with slightly different modulation frequencies HeLIC imaging ensues at the beat frequency (amplitude images only). The data acquisition card (NI USB-6259) in Fig. 2(b) is used to generate a reference signal and external trigger to the camera in an undersampling model [25]. The frame grabber (NI PCI-1427) is applied to scan images, sixteen of which are captured in one period. For temperature control, a Linkam LST 350 cryogenic stage is used that allows maintaining constant temperature in the range between 77 K and 520 K.

4. Results and discussion

Fig. 3(a) is a photograph of the as-synthesized multilayer CQD solar cell sample (structure shown in Fig. 1) with metallic Au contacts on the top. The bottom Au contact so labeled in Fig. 3(a) is connected to an indium tin oxide (ITO) conducting layer. Each golden circle-rectangle-shaped region, for example the one circumscribed in a dashed rectangle, represents a complete solar cell structure with top Au contact, while other regions with brown color are without top contact Au deposition. The highest power conversion efficiency (PCE) of this type of solar cell has been certified to be as high as 11.28% [1], while device performances vary from sample to sample due to factors such as electrical and mechanical defects introduced during various device fabrication processes, as well as film-inhomogeneity-associated short-circuit effects. As shown in Fig. 3(b), a HoLIC image of the corresponding solar cell sample in Fig. 3(a) reveals the charge carrier distribution within an entire solar device, thereby elucidating the influence of the Au electrode on charge carrier transport, and depicting the CQD solar cell inhomogeneity that originates from various defects. Regarding imaging, the CQD solar cell sample was flipped in a mirror reflection configuration to the photograph in Fig. 3(a). With the application of Au contacts in our CQD solar cells, an aluminum thin plate (with a smooth surface that can reflect light) was placed under the CQD solar cell to experimentally eliminate the potential Au-related reflection induced effects on HoLIC and HeLIC images. The HoLIC image in Fig. 3(b) demonstrates the negligible effect of Au-related reflection through the observation that even though identical Au electrodes are seen in Fig. 3(a), several Au-reflection regions exhibit HoLIC amplitudes that are almost the same as their surroundings without deposited Au electrodes. The solar cell contact electrode circumscribed within the dashed rectangle in Fig. 3(a) and (b) has a PCE of ca. 9%, Fig. 4, and has been further investigated using HeLIC and PCR. As shown in Fig. 4, both forward and reverse current –voltage scans are presented that show very little current-voltage hysteresis of our CQD solar cells.

Fig. 5 shows four electron transport parameter images reconstructed from Eq. (14) through computational best-fitting of 27 HeLIC amplitude images taken under excitation frequencies ranging from 100 Hz to

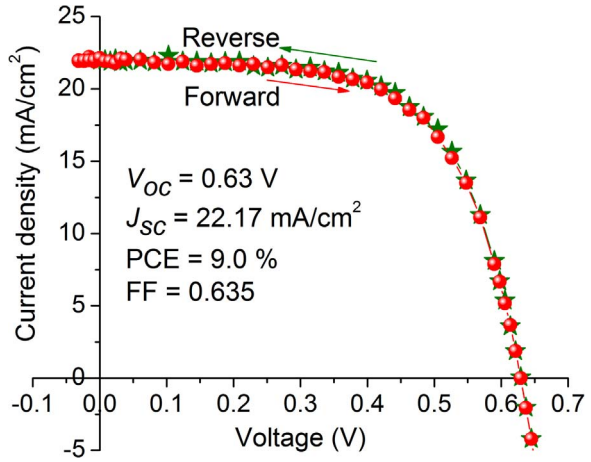

Fig. 4. Current-density-voltage characteristic of the CQD solar cell shown circumscribed by a dashed rectangle in Fig. 3(a). Both forward and reverse scans are shown.

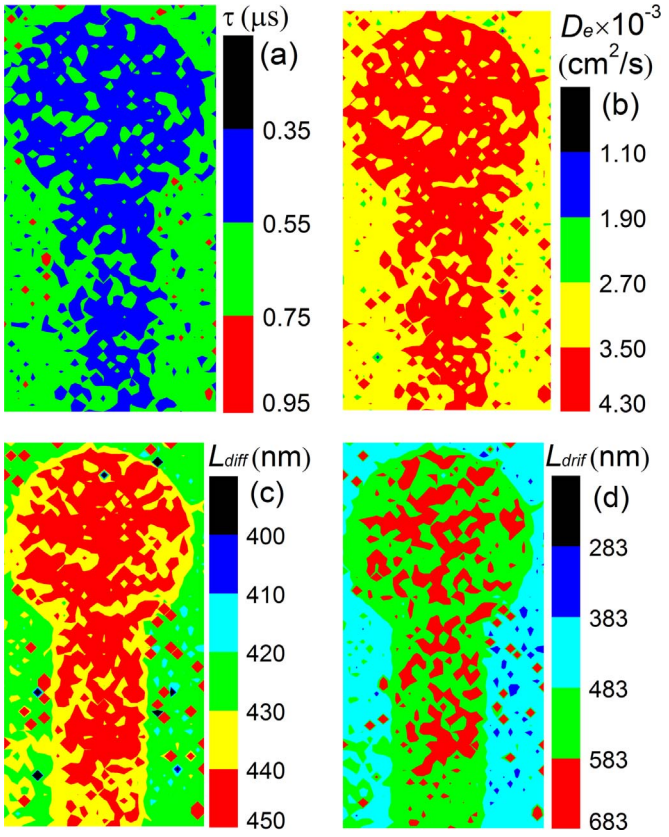

Fig. 5. Electron carrier lifetime τ (a), diffusivity D_e (b), diffusion length L_{diff} (c), and drift length L_{drif} (d) images of the circumscribed CQD solar cell A as shown in Fig. 3(a). The images are reconstructed using heterodyne lock-in carrierography image sequences in the frequency range from 100 Hz to 270 kHz. Eq. (14) was used for the extraction of the four parameters that constitute the images.

270 kHz. The distributions of electron lifetime τ, diffusivity D_e, and diffusion L_{diff} and drift L_{drif} lengths have been imaged for the solar cell electrode as circumscribed with a dashed rectangle in Fig. 3. These results offer insights on the CQD solar cell homogeneity, and on effects of the Au contact associated interface states on carrier transport dynamics. As tabulated in Table 1, other parameters involved in Eq. (14) were taken from the literature or measured experimentally. The lifetime image in Fig. 5(a) reveals lower τ values (0.35 μs–0.55 μs) for regions with than those without Au contacts, which can be attributed to the presence of enhanced trap state densities at Au/PbS-EDT interfaces. These trap states act as nonradiative recombination centers, dissipating energy, therefore, diminishing the overall carrier lifetime. These trap state enhancements at the metal/CQD interfaces can be reduced, first through improving the quality of the quantum dots themselves; second, through minimizing the effects of electrode contacts and the metal deposition processes. The CQD quality can be enhanced through surface materials chemistry [32,33] and improved synthesis methodologies [34,35]. For example, surface-passivation ligands with less mismatch to the dot lattice can be chosen [36], and solution-processed ligand exchange rather than solid-state exchange [1] can be applied and tested for CQD synthesis. Furthermore, although Au deposition was conducted at room temperature through thermal evaporation, using HeLIC imaging we found that in electrode contact-free regions the carrier lifetime also decreases after the thermal evaporation process for Au contact deposition. This is probably due to the surface damage incurred by the observed locally increased temperature and increased atomic collisions during the thermal evaporation process. Therefore, further investigation of the effects of the Au deposition process on CQD quality is recommended in a search for more robust CQD surface-passivation ligands that can endure local high temperature and atomic collisions during the contact deposition process.

In the framework of carrier hopping transport within CQD-based materials and devices, when energy disorder does not exceed the room temperature thermal energy kT, the character of carrier diffusion in CQD thin films can be treated as random which validates the mobility μ_e approximation using a three-dimensional random walk theory [37], i.e.

$$\mu_e = \frac{eL_{diff}^2}{kTn_{hop}}\frac{1}{\tau} \tag{16}$$

where n_{hop} is the average total number of the interdot hopping events an electron experiences before recombining radiatively or non-radiatively. Eq. (16) shows that μ_e increases with decreasing τ. Considering the hopping Einstein relation [2]

$$D_e = \frac{\mu_e kT}{exp\left(-\frac{E_a}{kT}\right)e} \tag{17}$$

in which E_a is the hopping activation energy, it can be seen that D_e also increases with decreasing τ, a fact mirrored in the diffusivity image of Fig. 5(b) which shows that the Au region possesses higher D_e. As for charge carriers, Eq. (16) predicts an electron diffusion length on the order of 10^2 nm that demonstrates the validity of diffusion length L_{diff} values in the image of Fig. 5(c) with higher L_{diff} in the Au regions. Although τ is lower in the Au regions, μ_e is expected to be higher using the random walk model, therefore, a tradeoff between lifetime and mobility

Table 1
Summary of the parameters used for heterodyne lock-in carrierography best-fits to Eq. (14).

Parameters	Electric field	Surface recombination velocity	Quantum yield	Incident photon intensity	Absorption coefficient	CQD thin film thickness
	E	S_j	η	I_0	β	d
Unit	V cm^{-1}	cm/s	1	J s^{-1} cm^{-2}	cm^{-1}	cm
Parameter values used for fitting	1.2 × 10^4	0	1	0.1 (1 sun)	10^7	3.6 × 10^{-5}
References and experimentally obtained parameters	$\frac{V_{oc}}{d_{solar\ cell}}$	ideal situation	ideal situation	experimentally measured	[27]	[1]

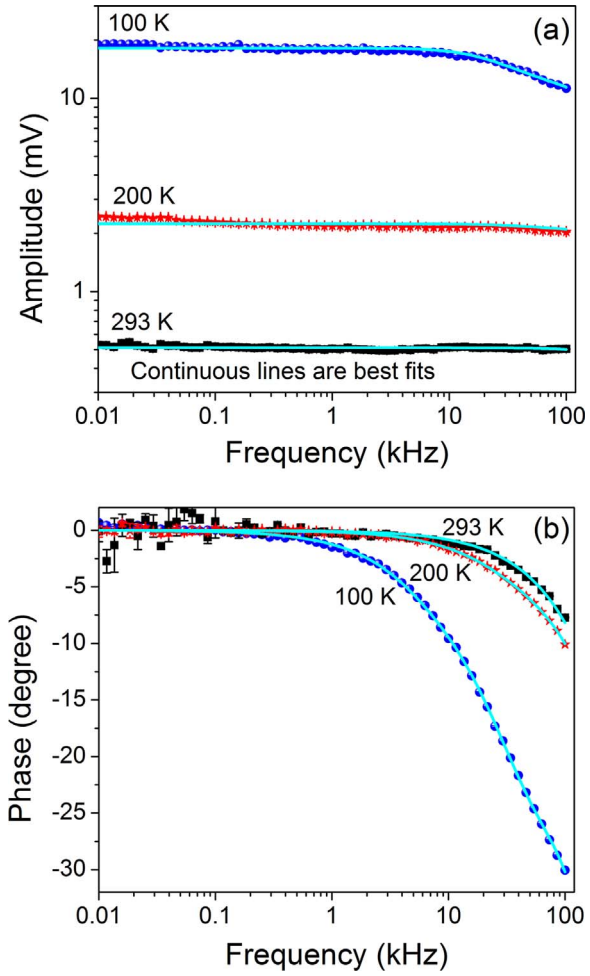

Fig. 6. PCR amplitude (a) and phase (b) of solar cell A shown circumscribed by a dashed rectangle in Fig. 3(a) at three temperatures. The best-fitting curves are obtained using Eq. (12).

results in higher drift length L_{drif} values as shown in Fig. 5(d). It should be noted that μ_e cannot be measured directly using this model. Although different regions in the HoLIC and HeLIC images exhibit amplitude contrast, the carrier transport parameters are not determined or affected by the absolute PL emission amplitude values of the solar cell. However, as further elaborated below, the "knee" frequency in Fig. 6, at which the PCR (same for HeLIC imaging) amplitudes start to decrease drastically, bears direct relationship to the carrier lifetime and other carrier transport parameters. The dynamic nature of the LIC and PCR techniques where quantitative information is extracted from the frequency response of the signals rules out any effects of Au-related reflection fluctuations across the surface on carrier transport parameter image construction and measurements.

PCR based on a single detector can be used for single spot measurements with a laser beam diameter of 3 mm which is the area of the circular tip of a single solar cell electrode as shown in Fig. 3. PCR amplitude and phase frequency scans on solar cell A in Fig. 3 are shown in Fig. 6(a) and (b), respectively. They resemble the HeLIC amplitude signal dependence on modulation frequency. As shown in Fig. 6(a), due to the reduced carrier-phonon interactions at low temperatures and a concomitant increase in the radiative emission rate accomplished by a decrease in the nonradiative decay rate, the PCR amplitude increases greatly at low temperatures. Correspondingly, higher carrier lifetimes at low temperatures yield an increased PCR phase lag compared to that at higher temperatures. The "knee" of a typical PCR amplitude and phase occurs at a frequency $f \sim 1/2\pi\tau$, reflecting a direct estimate of

Table 2
Summary of carrier lifetimes for three solar cell spatial regions in Fig. 3(a). A single InGaAs photodetector PCR was used for lifetime extraction through best-fitting the experimental data to Eq. (12).

Sample	Lifetime (μs)		
	100 K	200 K	293 K
A	17.07	0.43	0.30
B	5.66	0.36	0.24
C	26.35	8.05	0.30

carrier lifetime. The best-fitted carrier lifetimes using Eq. (12) at different temperatures for solar cells A and B, as well as in the region C without Au electrode contact shown in Fig. 3, are tabulated in Table 2. It is observed that carrier hopping lifetimes increase with decreasing temperature, indicating the phonon-assisted carrier hopping transport behavior of CQD-based materials and devices [2,6,25,27,38]. Carrier lifetime characterization using PCR further demonstrates that contact with the Au electrode diminishes the carrier hopping lifetime. For region C without Au contact, lifetimes significantly increase at low temperatures of 200 K and 100 K to 8.05 and 26.35 μs, respectively. Our *J-V* characteristics yield PCEs of solar cell B (8.4%) lower than that of A (9.0%), which is consistent with the lower lifetime of solar cell B when compared with A at all temperatures.

As a result, the PCR, HoLIC, and, especially, HeLIC technique can be very useful in solar cell manufacturing. For example, HeLIC can conduct fast, nondestructive, and contactless monitoring of in-line solar cell substrate and device homogeneity, providing qualitative information about product quality and entire surface image contrast dominated by the carrier lifetime distribution across the surface. Through more detailed analysis of multi-frequency image sets, large-area quantitative imaging of solar cell transport parameters associated with photovoltaic electrical properties can be reconstructed for more specific quality control of solar-cell products. Such photovoltaic parameter images are useful for further solar-cell efficiency optimization from materials screening to device processing and manufacturing method optimization in industry.

5. Conclusions

Fundamental carrier transport parameters and their distribution in CQD solar cells have been investigated for device PCE optimization purposes using HoLIC, HeLIC, and PCR as emerging dynamic quantitative interface non-destructive imaging methodologies, showing great potential for fundamental photovoltaic optoelectronic transport studies and industrial in-line or off-line manufactured large-area solar cell device characterization. Specifically, it was demonstrated that, compared with regions without Au contact, enhanced trap state density at the Au/CQD interface results in shorter electron carrier lifetime (ca. 0.5 μs), and higher diffusivity (ca. 4×10^{-3} cm^2/s), parameters that yield longer diffusion and drift lengths within the framework of a random walk hopping transport model.

Acknowledgements

The authors are grateful to the Natural Science and Engineering Research Council of Canada (NSERC) for a Discovery grant to A.M., and to the Canada Research Chairs Program.

References

[1] M. Liu, O. Voznyy, R. Sabatini, F.P.G. de Arquer, R. Munir, A.H. Balawi, X. Lan, F. Fan, G. Walters, A.R. Kirmani, S. Hoogland, F. Laquai, A. Amassian, E.H. Sargent, Hybrid organic-inorganic inks flatten the energy landscape in colloidal quantum dot solids, Nat. Mater. 16 (2016) 258–263.
[2] A. Mandelis, L. Hu, J. Wang, Quantitative measurements of charge carrier hopping

transport properties in depleted-heterojunction PbS colloidal quantum dot solar cells from temperature dependent current–voltage characteristics, RSC Adv. 6 (95) (2016) 93180–93194.
[3] A.G. Pattantyus-Abraham, I.J. Kramer, A.R. Barkhouse, X. Wang, G. Konstantatos, R. Debnath, L. Levina, I. Raabe, M.K. Nazeeruddin, M. Gratzel, E.H. Sargent, Depleted-heterojunction colloidal quantum dot solar cells, ACS Nano 4 (6) (2010) 3374–3380.
[4] X. Wang, G.I. Koleilat, J. Tang, H. Liu, I.J. Kramer, R. Debnath, L. Brzozowski, D.A.R. Barkhouse, L. Levina, S. Hoogland, E.H. Sargent, Tandem colloidal quantum dot solar cells employing a graded recombination layer, Nat. Photonics 5 (8) (2011) 480–484.
[5] I.J. Kramer, E.H. Sargent, The architecture of colloidal quantum dot solar cells: materials to devices, Chem. Rev. 114 (1) (2013) 863–882.
[6] L. Hu, A. Mandelis, X. Lan, A. Melnikov, S. Hoogland, E.H. Sargent, Imbalanced charge carrier mobility and Schottky junction induced anomalous current-voltage characteristics of excitonic PbS colloidal quantum dot solar cells, Sol. Energy Mater. Sol. Cells 155 (2016) 155–165.
[7] ⟨https://www.nrel.gov/pv/assets/images/efficiency-chart.png⟩ (Accessed 26 April 2017).
[8] M. Graetzel, R.A. Janssen, D.B. Mitzi, E.H. Sargent, Materials interface engineering for solution-processed photovoltaics, Nature 488 (7411) (2012) 304–312.
[9] M. Yuan, K.W. Kemp, S.M. Thon, J.Y. Kim, K.W. Chou, A. Amassian, E.H. Sargent, High-performance quantum-dot solids via elemental sulfur synthesis, Adv. Mater. 26 (21) (2014) 3513–3519.
[10] D. Zhitomirsky, O. Voznyy, L. Levina, S. Hoogland, K.W. Kemp, A.H. Ip, S.M. Thon, E.H. Sargent, Engineering colloidal quantum dot solids within and beyond the mobility-invariant regime, Nat. Commun. 5 (2014) 3803.
[11] S. Pradhan, A. Stavrinadis, S. Gupta, Y. Bi, F. Di Stasio, G. Konstantatos, Trap-state suppression and improved charge transport in PbS quantum dot solar cells with synergistic mixed-ligand treatments, Small (2017), http://dx.doi.org/10.1002/smll.201700598.
[12] M. Yuan, M. Liu, E.H. Sargent, Colloidal quantum dot solids for solution-processed solar cells, Nat. Energy 1 (2016) 16016.
[13] D. Zhitomirsky, I.J. Kramer, A.J. Labelle, A. Fischer, R. Debnath, J. Pan, O.M. Bakr, E.H. Sargent, Colloidal quantum dot photovoltaics: the effect of polydispersity, Nano Lett. 12 (2) (2012) 1007–1012.
[14] S. Xu, D. Thian, S. Wang, Y. Wang, F.B. Prinz, Effects of size polydispersity on electron mobility in a two-dimensional quantum-dot superlattice, Phys. Rev. B 90 (14) (2014) 144202.
[15] Y. Liu, M. Gibbs, J. Puthussery, S. Gaik, R. Ihly, H.W. Hillhouse, M. Law, Dependence of carrier mobility on nanocrystal size and ligand length in PbSe nanocrystal solids, Nano Lett. 10 (5) (2010) 1960–1969.
[16] T. Trupke, R.A. Bardos, M.C. Schubert, W. Warta, Photoluminescence imaging of silicon wafers, Appl. Phys. Lett. 89 (4) (2006) 044107.
[17] J.A. Giesecke, M.C. Schubert, B. Michl, F. Schindler, W. Warta, Minority carrier lifetime imaging of silicon wafers calibrated by quasi-steady-state photoluminescence, Sol. Energy Mater. Sol. Cells 95 (3) (2011) 1011–1018.
[18] Z. Hameiri, P. Chaturvedi, Spatially resolved electrical parameters of silicon wafers and solar cells by contactless photoluminescence imaging, Appl. Phys. Lett. 102 (7) (2013) 073502.
[19] M.D. Abbott, J.E. Cotter, F.W. Chen, T. Trupke, R.A. Bardos, K.C. Fisher, Application of photoluminescence characterization to the development and manufacturing of high-efficiency silicon solar cells, J. Appl. Phys. 100 (11) (2006) 114514.
[20] C. Shen, H. Kampwerth, M.A. Green, Photoluminescence based open circuit voltage and effective lifetime images re-interpretation for solar cells: the influence of horizontal balancing currents, Sol. Energy Mater. Sol. Cells 130 (2014) 393–396.
[21] C. Shen, H. Kampwerth, M. Green, T. Trupke, J. Carstensen, A. Schütt, Spatially resolved photoluminescence imaging of essential silicon solar cell parameters and comparison with CELLO measurements, Sol. Energy Mater. Sol. Cells 109 (2013) 77–81.
[22] K. Ramspeck, K. Bothe, D. Hinken, B. Fischer, J. Schmidt, R. Brendel, Recombination current and series resistance imaging of solar cells by combined luminescence and lock-in thermography, Appl. Phys. Lett. 90 (15) (2007) 153502.
[23] A. Mandelis, J. Batista, D. Shaughnessy, Infrared photocarrier radiometry of semiconductors: physical principles, quantitative depth profilometry, and scanning imaging of deep subsurface electronic defects, Phys. Rev. B 67 (20) (2003) 205208.
[24] J. Batista, A. Mandelis, D. Shaughnessy, Temperature dependence of carrier mobility in Si wafers measured by infrared photocarrier radiometry, Appl. Phys. Lett. 82 (23) (2003) 4077–4079.
[25] L. Hu, Z. Yang, A. Mandelis, A. Melnikov, X. Lan, G. Walters, S. Hoogland, E.H. Sargent, Quantitative analysis of trap-state-mediated exciton transport in perovskite-shelled PbS quantum dot thin films using photocarrier diffusion-wave nondestructive evaluation and imaging, J. Phys. Chem. C 120 (26) (2016) 14416–14427.
[26] Q. Sun, A. Melnikov, A. Mandelis, Camera-based high frequency heterodyne lock-in carrierographic (frequency-domain photoluminescence) imaging of crystalline silicon wafers, Phys. Status Solidi A 213 (2) (2016) 405–411.
[27] L. Hu, A. Mandelis, Z. Yang, X. Guo, X. Lan, M. Liu, G. Walters, A. Melnikov, E.H. Sargent, Temperature- and ligand-dependent carrier transport dynamics in photovoltaic PbS colloidal quantum dot thin films using diffusion-wave methods, Sol. Energy Mater. Sol. Cells 164 (2017) 135–145.
[28] L. Hu, M. Liu, A. Mandelis, A. Melnikov, E.H. Sargent, Colloidal quantum dot solar cell power conversion efficiency optimization using carrier hopping mobility and bandgap energy effects on current-voltage characteristics and electrode contact characterization using lock-in carrierography imaging, Prog. Photovolt. Res. Appl. (2017) 1–17, http://dx.doi.org/10.1002/pip.2920.
[29] A. Mandelis, Diffusion-Wave Fields: Mathematical Methods and Green Functions, Springer, New York, 2001, p. 584 Chapter 9.
[30] J. Nelson, The Physics of Solar Cells, Imperial College Press, London, 2003, p. 73 Chapter 3.
[31] M.A. Green, Solar Cells: Operating Principles, Technology, and System Applications, Prentice-Hall, Englewood Cliffs, 1982, p. 51 Chapter 3.
[32] X. Lan, O. Voznyy, A. Kiani, F.P. García de Arquer, A.S. Abbas, G.H. Kim, M. Liu, Z. Yang, G. Walters, J. Xu, M. Yuan, Passivation using molecular halides increases quantum dot solar cell performance, Adv. Mater. 28 (2) (2015) 299–304.
[33] Z. Ning, O. Voznyy, J. Pan, S. Hoogland, V. Adinolfi, J. Xu, M. Li, A.R. Kirmani, J.P. Sun, J. Minor, K.W. Kemp, Air-stable n-type colloidal quantum dot solids, Nat. Mater. 13 (8) (2014) 822–828.
[34] S.A. McDonald, G. Konstantatos, S. Zhang, P.W. Cyr, E.J. Klem, L. Levina, E.H. Sargent, Solution-processed PbS quantum dot infrared photodetectors and photovoltaics, Nat. Mater. 4 (2) (2005) 138–142.
[35] L. Turyanska, A. Patane, M. Henini, B. Hennequin, N.R. Thomas, Temperature dependence of the photoluminescence emission from thiol-capped PbS quantum dots, Appl. Phys. Lett. 90 (10) (2007) 101913.
[36] Z. Ning, X. Gong, R. Comin, G. Walters, F. Fan, O. Voznyy, E. Yassitepe, A. Buin, S. Hoogland, E.H. Sargent, Quantum-dot-in-perovskite solids, Nature 523 (7560) (2015) 324–328.
[37] N. Kholmicheva, P. Moroz, H. Eckard, G. Jensen, M. Zamkov, Energy transfer in quantum dot solids, ACS Energy Lett. 2 (1) (2016) 154–160.
[38] L. Hu, A. Mandelis, A. Melnikov, X. Lan, S. Hoogland, E.H. Sargent, Study of exciton hopping transport in PbS colloidal quantum dot thin films using frequency-and temperature-scanned photocarrier radiometry, Int. J. Thermophys. 38 (1) (2017) 7.